**ESAIM: PROCEEDINGS, Vol. ?, 2008, 1-10**
Editors: Will be set by the publisher

# SEPARATION OF SCALES IN AN ELASTIC INVERSE PROBLEM

H. Ammari[1], P. Garapon[2] and F. Jouve[3]

**Abstract.** Elastography is an imaging modality of Young's Modulus of a biological medium (breast, liver,...). It consists of vibrating a medium and infer from the observed wavefield the distribution of elasticity. The displacement field is observed in the all volume. It thus requires to solve an inverse problem. We present an optimization approach which solves the problem by minimizing a discrepancy functional. When we want to recover a complex inclusion in homogenous medium, we notice that the information contained in the wavefield should be decomposed into two parts, a near field close from the inclusion and a far field part away from it. As we justify theoretically and numerically, separating these scales allows us have a local and precise reconstruction.

**Résumé.** L'elastographie est une technique d'imagerie de l'élasticité des tissus du corps humain (sein, foie,...). Cela consiste à faire vibrer un milieu et à observer dans le volume le champ de déplacement induit, afin d'en déduire la carte de module d'Young. Il faut pour cela résoudre un problème inverse. Nous proposons une approche par optimisation qui maximise la vraisemblance entre un modèle numérique et les observations expérimentales. En voulant reconstruire une inclusion complexe, nous remarquons que l'information contenue dans le champ de déplacement se sépare en deux termes, de champs proche au voisinage de l'inclusion, et de champ lointain à grande distance du défaut. Nous justifions théoriquement et numériquement qu'il est profitable de séparer ces deux informations pour obtenir une reconstruction locale et précise.

## Introduction

Mechanical response of living tissues is a wide source of information in medical science. Echography, is an example of situation where one exploits the response of a tissue to a compressional or sound wave. It provides information on a specific contrast, which is mainly anatomic. That is why echography is often used to image structures in the body. The stiffness of tissues provides very interesting clinical information: it helps discriminate between benign and malignant lesions in the breast, it helps diagnosis liver fibrosis, it can monitor muscle fine muscular activity,... Yet, this stiffness, or shear modulus is not related in general to the compressional modulus, and thus is invisible to echography.

The static way to understand shear modulus is to ask the following question: suppose you shear a tissue with a static force, what is the amplitude of the transverse displacement that will occur ? The relationship between the observed displacement and the applied stress, will give an estimate of the shear modulus. The interpretation of compressional response would be to apply a compression force on tissue and measure the change in volume. For the case of biological tissues, this is very different from the previous interpretation. The dynamic interpretation of the shear modulus is the following: suppose you apply dynamic shear in the medium

[1] ammari@cmapx.polytechnique.fr, Centre de Mathématiques Appliquées, Ecole Polytechnique, 91128 Palaiseau, France.
[2] pierre.garapon@espci.fr, Centre de Mathématiques Appliquées, Ecole Polytechnique, 91128 Palaiseau, France.
[3] jouve@math.jussieu.fr, Laboratoire J.L. Lions, Université Paris VII, Denis Diderot, 75252 Paris, France.

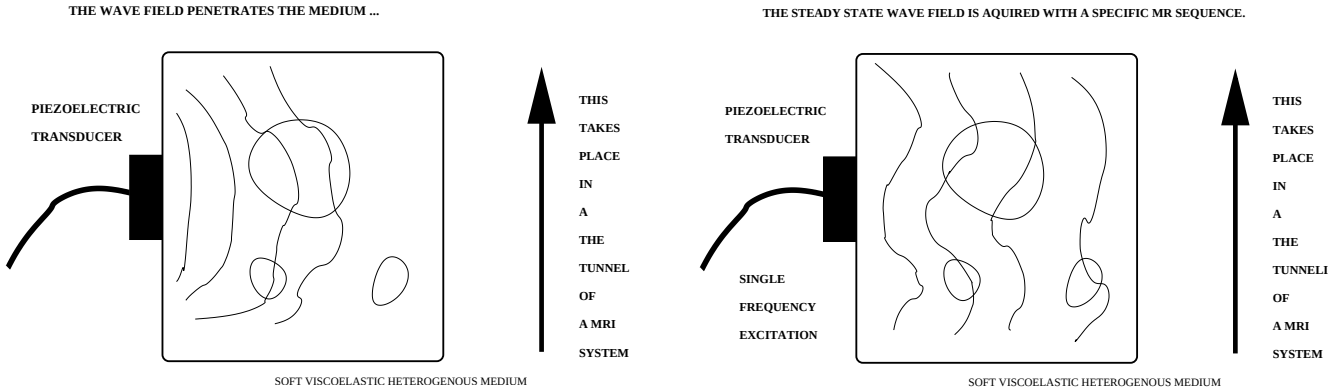


FIGURE 1. Vibrating the medium at a single frequency induces a stationary elastic field in the medium.

(an impulse or an harmonic excitation), what will be the resulting displacement? If one have access to this displacement, one could solve an inverse problem and have access to the shear modulus. This is the principle of elastography. It thus relies on three steps: apply dynamic shear to a tissue, measure displacement and solve an inverse problem to get a map of Young's modulus. Each one of these three steps is a technical challenge by itself: Applying dynamic shear to tissues can be done by simply vibrating a piezoelectric transducer on a body, which is the technique used in Magnetic Resonance Elastography. But the shear may not transmit well to the interesting part of tissues, because it may be disturbed by surface layers of fat or bones. One has suggested to induce remotely shear in tissues by focusing an ultrasonic beam; see [7]. These techniques induce a wavefield $\mathbf{u}^*$ in the medium. The imaging part is also a technical challenge because it needs to **remotely** image the wavefield in the medium. One could use a specific Magnetic Resonance sequence that track displacements; see [4]. That is the technique we are interested in. But one could also record this wavefield remotely using ultra-fast echography; see [7]. The inverse problem is how to recover the shear modulus map $\mu(x)$ from the measurements of the field $\mathbf{u}$. This is the problem we are going to discuss. The paper is organized as follows: We present the mathematical framework in section 1. In section 2, we present a multi-scale argument. Finally, we discuss the numerical results and their stability in section 3.

## 1. The inverse problem of elastography

### 1.1. Mathematical Model

The experimental setting we try to model in briefly described in Fig. 1, the experimental results obtained by R. Sinkus's group are shown in Fig. 2. Here $\Omega$ will be the biological set we want to investigate, $\Gamma_1$ and $\Gamma_2$ are parts of boundary of this domain, which are respectively the interface which we vibrate, and the part of the boundary which is constraint free. The mechanical modelling of biological media chosen here is the linear, continuous, and incompressible elasticity system. The incompressibility assumption is justified by the great difference observed experimentally between the two Lamé parameters $\lambda$ and $\mu$. In soft media, $\lambda \approx 10^9 Pa$ and $\mu \approx 10^3 Pa$, so the incompressible assumption is justified. In this context, the Young's modulus is related to the shear modulus $E \approx 3\mu$ so mapping one or the other is equivalent.

Let $\mathbf{e}(\mathbf{v}) = \frac{1}{2}(\nabla \mathbf{v} + \nabla \mathbf{v}^{\mathbf{T}})$ be the strain tensor, $\mathbf{A}[\mathbf{X}] = \lambda Tr(\mathbf{X})\mathbf{I} + 2\mu\mathbf{X}$ be the stress-strain relationship, and let $\nu$ be the outward unit normal to $\partial\Omega$. One can prove that as $\lambda \to \infty$, the solution $\mathbf{v}$ of the following elasticity system:

$$\begin{cases} \nabla.\mathbf{A}[\mathbf{e}(\mathbf{v})] + \rho\omega^2\mathbf{v} = \mathbf{0} \quad \text{in} \quad \mathbf{\Omega}, \\ \mathbf{v} = F \quad \text{in} \quad \Gamma_1, \\ \mathbf{A}[\mathbf{e}(\mathbf{u})]\nu = 0 \quad \text{in} \quad \Gamma_2, \end{cases} \tag{1}$$

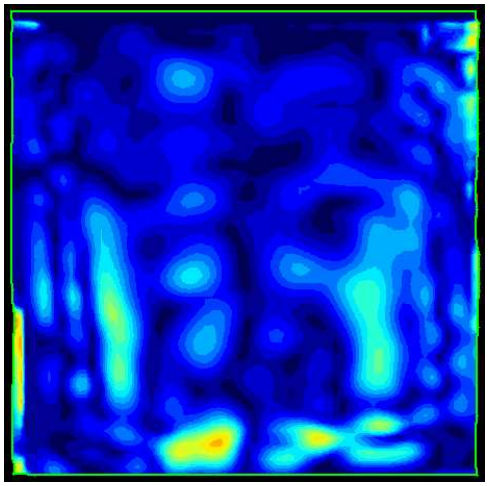

FIGURE 2. Experimental wavefield into a biomedical phantom. The displacement are acquired by an elastoraphy MR sequence (R. Sinkus's group - LOA). the transducer is at the bottom, one notices that although the waves are visible, the amplitude decay in the vertical direction, because of a slight viscosity of the tissue.

converges to $\mathbf{u}$ defined by:

$$\begin{cases} \nabla.(\mu(x)\mathbf{e}(\mathbf{u})) + \rho\omega^2\mathbf{u} + \nabla p = 0 \quad \text{in} \quad \Omega, \\ \nabla.\mathbf{u} = 0 \quad \text{in} \quad \Omega, \\ \mathbf{u} = F \quad \text{in} \quad \Gamma_1, \\ \mathbf{e}(\mathbf{u})\nu = 0 \quad \text{in} \quad \Gamma_2. \end{cases} \tag{2}$$

### 1.2. Setting of the inverse problem

We consider the following inverse medium problem: Suppose the solution $\mathbf{u}$ to (2) is known in the all domain $\Omega$, is it possible to recover a map of the shear modulus $\mu(x)$ ?

Previous works in the Elastography community have proposed a local reconstruction based on an explicit inversion formula: Let $\mathbf{q}$ be the rotational of $\mathbf{u}$, $\mathbf{q} = \nabla \times \mathbf{u}$ then

$$\mu = -\frac{\rho\omega^2\mathbf{q}}{\Delta\mathbf{q}}.$$

This formula is local but has to overcome a major stability issue, computing the terms $\Delta\nabla\times\mathbf{u}$ and $\nabla\times\mathbf{u}$ being very unstable. Moreover, this models assumes the shear modulus $\mu$ to be locally homogenous, so this method is *a priori* of low resolution to reconstruct sharp contrasts, and jumps. That is indeed what is observed in practice. We suggest to address the problem by minimizing the discrepancy functional between the observation field and the synthetic field computed according to model (2), that is $J(\mu) = ||\mathbf{u}_{exp} - \mathbf{u}_{model}||^2_{L^2(\Omega)}$. This means that the estimated shear modulus map $\hat{\mu}$ is optimal to match the model with the experiment over the all domain $\Omega$. This a very natural and widely used approach in inverse problem theory. It can be seen the natural extension of impedance imaging procedures. This approach has been investigated by the biomedical community, for instance in [9, 10].

### 1.3. Optimization of the discrepancy functional

If one wants to minimize the functional $J(\mu) = ||\mathbf{u}^* - \mathbf{u}(\mu)||^{\mathbf{2}}_{\mathbf{2}}$, one is interested in computing the gradient of the functional $\frac{\partial J}{\partial \mu}$. The variational formulation of (2), together with the lifting of the boundary condition into an external force $\tilde{f}$, allows us to rewrite the minimization program:

$$\begin{cases} Min\ J(\mu) = ||\mathbf{u}^* - \mathbf{u}(\mu)||^{\mathbf{2}}_{\mathbf{2}} \\ \text{and} \displaystyle\int_\Omega \mu\ \mathbf{e}(\mathbf{u}) : \mathbf{e}(\mathbf{v}) + \rho\omega^2\mathbf{u}.\mathbf{v}dx = \int_\Omega \tilde{f}.\mathbf{v}\ dx, \quad \forall v \in H_{div}, \end{cases} \tag{3}$$

where $H_{div} = \{\mathbf{v} \in H_0^1 \text{ such that } \nabla.\mathbf{v} = 0\}$.

We write an alternative augmented lagrangian formulation that relaxes the constraint:

$$\tilde{J}(\mathbf{u}, \mathbf{v}, \mu) = J(\mu) + \int_\Omega \mu(x)\mathbf{e}(\mathbf{u}) : \mathbf{e}(\mathbf{v})(x) + \rho\omega^2 \mathbf{u}.\mathbf{v}(x)dx - \tilde{f}.v \; dx.$$

It follows that $J(\mu) = \tilde{J}(u(\mu), \mathbf{v}, \mu)$. The chain rules thus gives

$$\frac{\partial J}{\partial \mu} = \mu \; \mathbf{e}(\mathbf{u}) : \mathbf{e}(\mathbf{v}) \text{ as long as } \frac{\partial \tilde{J}}{\partial \mathbf{u}} \equiv 0.$$

This last condition determines the adjoint parameter $v$:

$$\forall h \in H_{div}, \quad \int_\Omega (\mathbf{u} - \mathbf{u}^*).h = \int_\Omega \mu \mathbf{e}(h) : \mathbf{e}(v) + \rho\omega^2 h.v.$$

We can consequently summarize the gradient of the discrepancy functional as follows:

$$\begin{cases} \frac{\partial J}{\partial \mu} = \mu \; \mathbf{e}(u) : \mathbf{e}(v) \; , \\ \\ \nabla.(\mu(x)\nabla \mathbf{u}) + \rho\omega^2 \mathbf{u} + \nabla \mathbf{p} = \mathbf{f} \quad \nabla.\mathbf{u} = \mathbf{0} \; , \\ \\ \nabla.(\mu(x)\nabla \mathbf{v}) + \rho\omega^{\mathbf{2}} \mathbf{v} + \nabla \mathbf{q} = (\mathbf{u} - \mathbf{u}^*) \quad \nabla.\mathbf{v} = \mathbf{0} \; . \end{cases} \tag{4}$$

## 1.4. **Numerical implementation**

We implemented this gradient descent method with the following loop:

- Initialization: Set initial guess $\mu_0$ to be homogenous. Compute the initial forward problem $\mathbf{u}(\mu_0)$, compute the initial cost function $||\mathbf{u}^* - \mathbf{u}(\mu_0)||_2^2$, compute the inital adjoint problem $\mathbf{v_0}$, and set initial descent parameter $\delta_0$.
- Main loop: For a certain number of iterations $N$: compute the gradient $\mu_n(x)\mathbf{e}(\mathbf{u_n}) : \mathbf{e}(\mathbf{v_n})$. Compute the new forward and adjoint fields $\mathbf{u}_{n+1}$, $\mathbf{v_{n+1}}$, associated to $\mu_{n+1} = \mu_n + \delta_n \mu_n(x)\mathbf{e}(\mathbf{u_n}) : \mathbf{e}(\mathbf{v_n})$ . Compute the new cost function $J_{n+1} = ||\mathbf{u}^* - \mathbf{u}(\mu_{n+1})||_2^2$.
  If $J_{n+1} < J_n$ then set $\delta_{n+1} = \delta_n * (1.1)$ and $\mu_{n+1} = \mu_{n+1}$.
  if $J_{n+1} > J_n$ then set $\delta_{n+1} = \delta_n * (0.5)$ and $\mu_{n+1} = \mu_n$.
- End: End the loop after a fixed number of iterations, or when the cost becomes smaller than a given parameter $\epsilon$.

Notice that we used an "adaptative" step amplitude $\delta$ to enforce the decrease of the functional by diminishing the step. When the descent seems to be efficient, one increases the step size. This is somehow dichotomy in order to find an optimal step size for each iteration. Even though the idea seems very standard, we still observed some speed up of the descent. Yet, the convergence speed of the algorithm was of course far from being optimal, as one could guess as far as we use a basic gradient descent method. We think of speeding up the method with Newton or Quasi Newton methods, but this remains to be implemented.

## 1.5. **Numerical illustration**

To perform our computations, we used the "SOL" FEM solver developed by the third author. We implemented 2D examples on rectangular meshes of rectangular elements. We typically used 140×140 meshes and each computation (forward or adjoint) took approximately 20 seconds on a dual core processor. The "experimental" field obtained numerically are shown in Fig. 3, together with the reconstruction results.

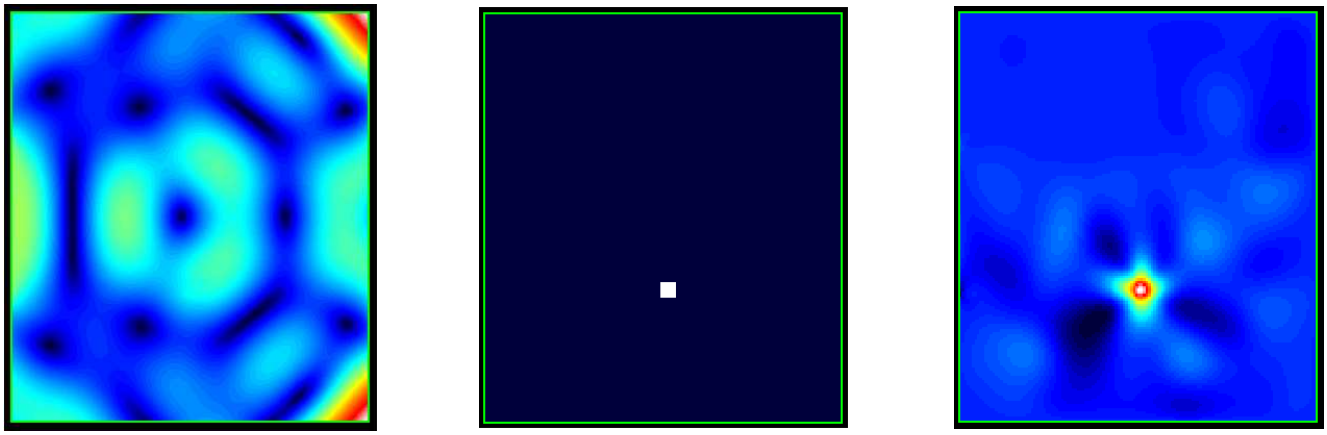

FIGURE 3. The numerically simulated displacement field on the left, the actual shear modulus map in the middle, and the reconstructed map on the right.

### 1.6. **Recovery of details**

Suppose we want to recover a more complex map, like a small inclusion of different shear modulus $\tilde{\mu}$, of complex shape in homogenous background of shear modulus $\mu$. Such a situation, similar to the one encountered in Fig. 4, corresponds to the scheme in Fig. 5. If we want to recover a more complex map of shear modulus, the algorithm seems to be less efficient as shown in Fig. 4. The reason for this is that the information contained in the far field and close field is completely different because of the diffraction property of the wave propagation. The propagation filters all the rapid spatial oscillations in the far field. One could see that by decomposing a solution $\mathbf{w}(\mathbf{r},\theta)$ of the Helmholtz equation $(\Delta+\omega^2)\mathbf{w}=0$ in 2D, scattered from a complex object, and satisfying a radiation condition:

$$\mathbf{w}(r,\theta)=\sum \mathbf{w}_n H_n(\omega r)e^{in\theta}.$$

where $H_n$ are Hankel's functions. The rapid angular oscillations associated to high values of $n$, are associated to rapidly decaying $H_n$. The relevant parameter to quantify this decay is $\omega r$, which means that the characteristic decay length is determined by the wavelength $\Lambda=\frac{2\pi}{\omega}$.

Thus the algorithm performs a bad trade off between the far field reconstruction and near field reconstruction. In fact, one could decompose the discrepancy functional over the all domain in two parts:

$$J(\mu)=\sum_{\text{close field}}||\mathbf{u}^*-\mathbf{u}||^2+\sum_{\text{far field}}||\mathbf{u}^*-\mathbf{u}||^2.$$

But these two parts have different minimizers, for the intrinsic reason that the information carried in the near and far field parts of $\mathbf{u}^*$ are different. As we will see in the next section, the only information that travels away from the inclusion is a kind of polarization tensor (which we have called in [1] Viscous Moment Tensor), and the reconstructed inclusion should be an equivalent ellipse. But in the near field, the perturbation is the solution of a problem, which is well posed in the sense that the near field is one to one with the corresponding shape and contrast of the inclusion.

For this reason, we want to separate the two scales in order to coherently treat each part of the information.

## 2. SCALE SEPARATION IN THE INVERSE PROBLEM

We introduce two scales in the problem as illustrated in Fig. 5. The small spatial scale is associated to a near variable $\xi=\frac{x-z}{\epsilon}$. It will characterize the perturbation due to the inclusion, in a small region around $z$. The large variable is associated to perturbation far from the object. In order to formally derive the two scale

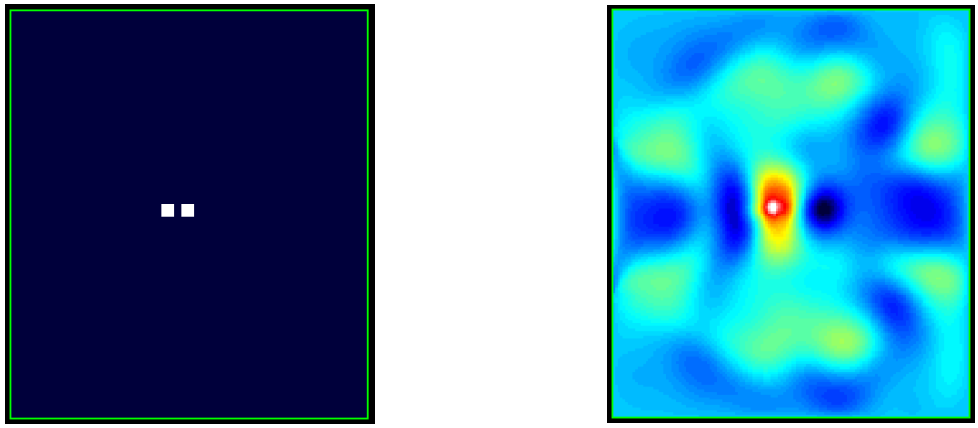

FIGURE 4. Actual and recovered map in the case of a complex map. We fail to recover accurately the details form the far field measurements.

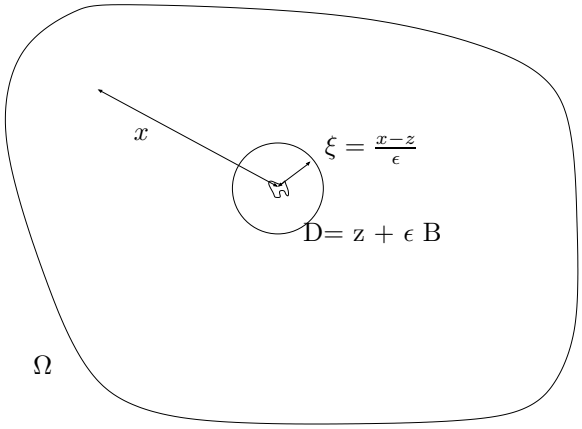


FIGURE 5. We introduce two scales to capture the different nature of the perturbation near the inclusion, and far from the inclusion.

asymptotics when the dimensions of the perturbation $\epsilon$ goes to 0, we introduce an Ansatz development for the perturbed elastic field. Suppose $\mathbf{u}$ is the solution to:

$$\begin{cases} (\mu\Delta + \omega^2\rho)\mathbf{u} + \nabla p = 0 \quad \text{in } \Omega - \overline{D}, \\ (\tilde{\mu}\Delta + \omega^2\rho)\mathbf{u} + \nabla p = 0 \quad \text{in } D, \\ \mathbf{u}|_- = \mathbf{u}|_+ \quad \text{on } \partial D, \\ (p|_+ - p|_-)\mathbf{N} + \mu\frac{\partial \mathbf{u}}{\partial \mathbf{N}}|_+ - \tilde{\mu}\frac{\partial \mathbf{u}}{\partial \mathbf{N}}|_- = 0 \quad \text{on } \partial D, \\ \nabla.\mathbf{u} = 0 \quad \text{in } \Omega, \\ \mathbf{u} = F \quad \text{on } \Gamma_1, \\ \frac{\partial \mathbf{u}}{\partial \nu} = 0 \quad \text{on } \Gamma_2, \end{cases} \tag{5}$$

where $\frac{\partial}{\partial \mathbf{N}}$ denotes $\frac{1}{2}(\frac{\partial}{\partial \mathbf{n}} + \frac{\partial}{\partial \mathbf{n}}^T)$ and $\mathbf{n}$ is the outward unit normal to $\partial D$. One verifies that (5) is the same equation as (2), in the case where $\mu$ is piecewise constant, and has a different value $\tilde{\mu}$ in the inclusion. To see this, one could use the weak formulation of (2) and integrate by parts in order to obtain the transmission conditions. Then we set the following *a priori* inner and outer expansions, that correspond to the perturbed

near and far field:

$$\begin{cases} \mathbf{u}(x) = U_0(x) + \epsilon U_1(x) + \epsilon^2 U_2(x) + \dots \\ \\ \hat{\mathbf{u}}(\xi) = \mathbf{v}_0(\xi) + \epsilon \mathbf{v}_1(\xi) + \epsilon^2 \mathbf{v}_2(\xi) + \dots \\ \\ \lim\limits_{x\to 0} \mathbf{u}(x) = \lim\limits_{|\xi|\to\infty} \hat{\mathbf{u}}(\xi). \end{cases} \tag{6}$$

One assume the same kind of expansion for the pressure field $p$, which we omit to write, as we focus on the displacement field $\mathbf{u}$. If we input this Ansatz in equation (5) and change variables $x \to \frac{x-z}{\epsilon}$. We see when identifying the terms in $\epsilon^{-2}$ and $\epsilon^{-1}$ that:

$$\hat{\mathbf{u}}(\xi) = \mathbf{U}_{\mu=\tilde{\mu}}(z) + \epsilon \hat{\mathbf{v}}(\xi) + O(\epsilon^2),$$

where $\hat{\mathbf{v}}$ is defined by:

$$\begin{cases} \mu \Delta \hat{\mathbf{v}} + \nabla \hat{p} = 0 \quad \text{in } \Omega - \overline{D}, \\ \tilde{\mu} \Delta \hat{\mathbf{v}} + \nabla \hat{p} = 0 \quad \text{in } D, \\ \hat{\mathbf{v}}|_- = \hat{\mathbf{v}}|_+ \quad \text{on } \partial D, \\ (\hat{p}|_+ - \hat{p}|_-)\mathbf{N} + \mu \frac{\partial \hat{\mathbf{v}}}{\partial \mathbf{N}}|_+ - \tilde{\mu} \frac{\partial \hat{\mathbf{v}}}{\partial \mathbf{N}}|_- = 0 \quad \text{on } \partial D, \\ \nabla . \hat{\mathbf{v}} = 0 \quad \text{in } \Omega, \end{cases} \tag{7}$$

subject to the matching conditions:

$$\begin{cases} \hat{\mathbf{v}}(\xi) - \nabla \mathbf{U}_{\mu=\tilde{\mu}}(z)\xi \to 0 \quad as \quad |\xi| \to \infty, \\ \hat{p}(\xi) \to 0, \quad as \quad |\xi| \to \infty, \end{cases} \tag{8}$$

which couple the inner and outer expansions. Condition (8) corresponds to

$$\lim_{x\to 0} \mathbf{u}(x) = \lim_{|\xi|\to\infty} \hat{\mathbf{u}}(\xi).$$

For the far field asymptotic expansion, we notice that the difference between the perturbed field and the background field $\mathbf{U}_0$, which is the field when $\tilde{\mu} = \mu$, verifies the following system:

$$\begin{cases} (\Delta + \kappa^2)(\mathbf{u} - \mathbf{U}_0) + \dfrac{1}{\mu}\nabla(p - q_0) = 0 \quad \text{in } \Omega \setminus \overline{D}, \\ \\ (\Delta + \kappa^2)(\mathbf{u} - \mathbf{U}_0) + \dfrac{1}{\mu}\nabla(p - q_0) = (\kappa^2 - \tilde{\kappa}^2)\mathbf{u} + \left(\dfrac{1}{\mu} - \dfrac{1}{\tilde{\mu}}\right)\nabla p \quad \text{in } D, \\ (\mathbf{u} - \mathbf{U}_0)\big|_+ - (\mathbf{u} - \mathbf{U}_0)\big|_- = 0 \quad \text{on } \partial D, \\ \dfrac{1}{\mu}(p - q_0)\big|_+ \mathbf{N} + \dfrac{\partial}{\partial \mathbf{N}}(\mathbf{u} - \mathbf{U_0})\big|_+ \\ \quad = \dfrac{1}{\mu}(p - q_0)\big|_- \mathbf{N} + \dfrac{\partial}{\partial \mathbf{N}}(\mathbf{u} - \mathbf{U_0})\big|_- + \dfrac{\tilde{\mu} - \mu}{\mu}\dfrac{\partial \mathbf{u}}{\partial \mathbf{N}}\big|_- \quad \text{on } \partial \mathbf{D}, \\ \nabla \cdot (\mathbf{u} - \mathbf{U}_0) = 0 \quad \text{in } \Omega, \\ \mathbf{u} - \mathbf{U}_0 = 0 \quad \text{on } \partial\Omega, \end{cases} \tag{9}$$

where $\kappa = \frac{\rho\omega}{\mu}$ and $\tilde{\kappa} = \frac{\rho\omega}{\tilde{\mu}}$. Integrating over $y \in \Omega \setminus \overline{D}$ the first equation in (9) against Green's function $\mathbf{G}^i(x, y)$, which is defined by

$$\begin{cases} (\mu \Delta_y + \omega^2 \rho)\mathbf{G}^i(x, y) + \nabla \pi = \delta_{y=x}\mathbf{e_i}, \\ \\ \nabla_y . \mathbf{G}^i(x, y) = 0, \end{cases} \tag{10}$$

and using the divergence theorem, we obtain the following representation formula for $x \in \Omega$:

$$\mathbf{u}(x) = \mathbf{U}_0(x) + (\frac{\tilde{\mu}}{\mu} - 1) \int_{\partial D} \mathbf{G}(x, y) \frac{\partial \mathbf{u}}{\partial \mathbf{N}}\bigg|_- (y)\, d\sigma(y) + (\frac{1}{\mu} - \frac{1}{\tilde{\mu}}) \int_D \mathbf{G}(x, y) \nabla p(y)\, dy,$$

where $\mathbf{GX} = \sum_{i,j} \mathbf{e}_i \mathbf{G}^i_j \mathbf{X}_j$ and $\mathbf{G}^i_j$ is the $j$-th component of $\mathbf{G}^i$.
Since

$$\left(\frac{\tilde{\mu}}{\mu} - 1\right) \int_{\partial D} \frac{\partial \mathbf{u}}{\partial \mathbf{N}}\Big|_{-} (y)\, d\sigma(y) + (\frac{1}{\mu} - \frac{1}{\tilde{\mu}}) \int_D \nabla p(y)\, dy = -\left(\frac{\tilde{\mu}}{\mu} - 1\right) \kappa^2 \int_D \mathbf{u}\, dy,$$

as it can be seen by integration by parts, we obtain from the inner expansion that for $x$ far away from $z$, in $\mathbb{R}^2$,

$$\mathbf{u}_0(x) \approx \mathbf{U}_0(x) + \epsilon^2 \sum_{i,j,\ell=1}^{2} \mathbf{e}_i \partial_\ell \mathbf{G}^i_j(x,z) \Big[ (\frac{\tilde{\mu}}{\mu} - 1) \int_{\partial B} \left(\frac{\partial \hat{\mathbf{v}}}{\partial \mathbf{N}}\right)_j \Big|_{-} (\xi) \xi_\ell \, d\sigma(\xi) \quad + \quad (\frac{1}{\mu} - \frac{1}{\tilde{\mu}}) \int_B \partial_j \hat{p}(\xi) \xi_\ell \, d\xi \Big].$$

which may simplify as follows:

$$\mathbf{u}_0(x) \approx \mathbf{U}_0(x) + \epsilon^2 (\frac{\tilde{\mu}}{\mu} - 1) \sum_{i,j,\ell=1}^{2} \mathbf{e}_i \partial_\ell \mathbf{G}^i_j(x,z) \Big[ \int_B \mathbf{e}(\hat{\mathbf{v}})_{j,\ell}(\xi)\, d\sigma(\xi) \Big].$$

where $\mathbf{E}$ is defined in (2).
The quantity $\int_B \mathbf{e}(\hat{\mathbf{v}})_{j,\ell}(\xi)\, d\sigma(\xi)$ is closely related to the Viscous Moment Tensor $(V^{p,q}_{j,\ell})_{j,\ell,p,q}$ we defined in [1]:

$$\mathbf{V}(B)_{j,\ell} = \int_B \mathbf{e}(\hat{\mathbf{v}})_{j,\ell}(\xi)\, d\sigma(\xi) = \partial_p \mathbf{U}^q_0 V^{p,q}_{j,\ell}.$$

This notion of Viscous Moment Tensors generalizes the notion of polarization tensor. The rigorous proof of convergence for these asymptotics are based on adequate layer potential analysis, and can be found in [1]. One could summarize these asymptotics as follows:

$$\begin{cases} \hat{\mathbf{u}}(\xi) \approx \mathbf{U}_{\mu=\tilde{\mu}}(z) + \epsilon.\hat{\mathbf{v}}(\xi) \quad \text{in the near field,} \\ \\ \mathbf{u}(x) \approx \mathbf{U}_{\mu=\tilde{\mu}}(x) + \epsilon^2 (\frac{\tilde{\mu}}{\mu} - 1) \nabla \mathbf{G} : \mathbf{V}(B) \quad \text{in the far field.} \end{cases} \tag{11}$$

We stress the following points:

- Although it decays rapidly with the volume of the defect, there exists a coupling between a local perturbation at the location $z$ and the far field everywhere in the domain.
- As expected, the far field perturbation carries a less accurate information since the field $\hat{\mathbf{v}}$ is integrated over the boundary of $B$ and it is multiplied by $\nabla \mathbf{G}$, whereas the near field carries a more accurate information.
- The fact that there is no uniform asymptotics for the perturbed field over the all domain, show that it is impossible to do good inverse processing of the data on the all domain, one has to perform **local reconstruction**. We exploit this fact by running the method on a subregion just around the suspected defect.

We observe that indeed, we achieved to coherently treat the different scales as we get a reconstruction which is pixelwise; see Fig. 6. Indeed, as suggested by our mathematical analysis, the resolution of the local method is essentially the spatial resolution of the imaging system, that is the resolution with which $\mathbf{u}^*$ is acquired. That is what we see in the numerical test. Indeed, previous result suggest that if the data is completely scalable (suppose you have infinite spatial resolution for $\mathbf{u}^*$) and no noise is added, you can reconstruct $\mu$ with infinite precision. As far as there is a certain scaling where $\mu_{\text{rescaled}}$ has the morphology of Fig. 5, one transforms the data in the same scaling, and one will end up with a problem where the gradient descent gives satisfactory results. Of course in practice, the limitations are the sampling density, and the noise. In practical cases, the sampling density is the main limiting factor; see [10].

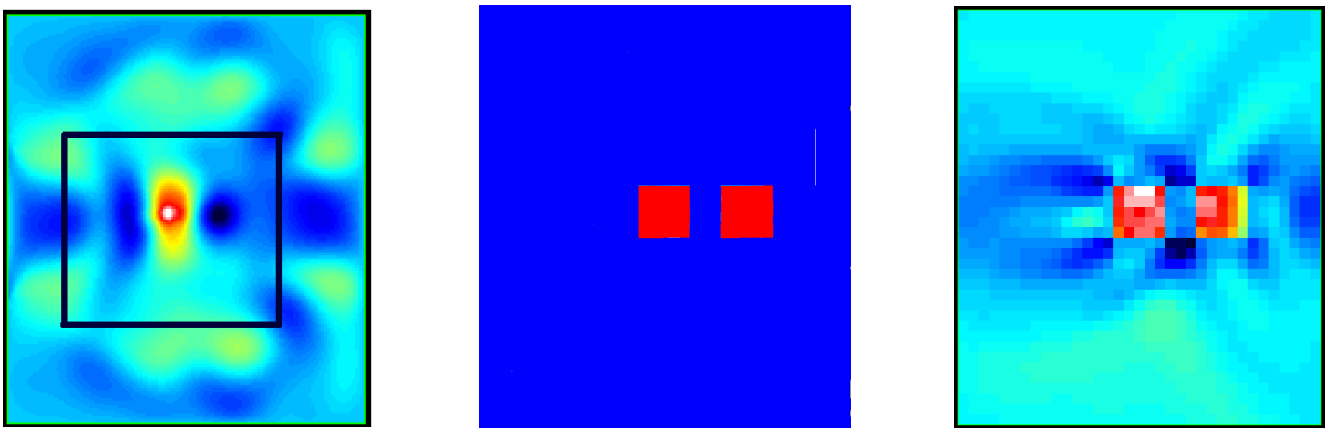

FIGURE 6. Reconstruction without separation of scales on the left, a zoom on the inclusion to recover in the middle, and on the right the reconstruction limited on the subregion defined by the full black line on the left.

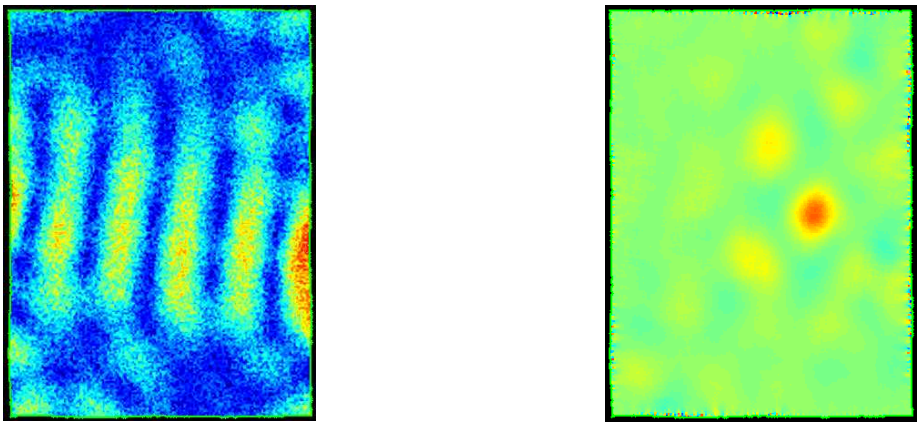

FIGURE 7. Elastic field with 35 % noise, and reconstruction of an inclusion. Although the data is noisy, the inclusion is still visible.

## 3. STABILITY OF THE METHOD

We discuss the stability of the reconstruction method when noise is added to the data. We added random gaussian noise on each pixel with no correlation from a pixel to another, we then ran the reconstruction on these noisy sets.

### 3.1. **Stability of the "global" and "local" reconstruction method**

When we reconstructed the shear modulus from the data from the all domain $\Omega$ (that is without scale separation), we observed that the method was quite robust.

This stability feature is due to the fact that the spatial frequencies which dominate in the data are mostly of the order of $k = \frac{1}{\omega}$, whereas the noise is uncorrelated and thus features very high spatial frequencies. The algorithm is thus marginally disturbed by the noise. This causes the efficient noise to be reduced, and the problem to be better posed in the "sense of stability".

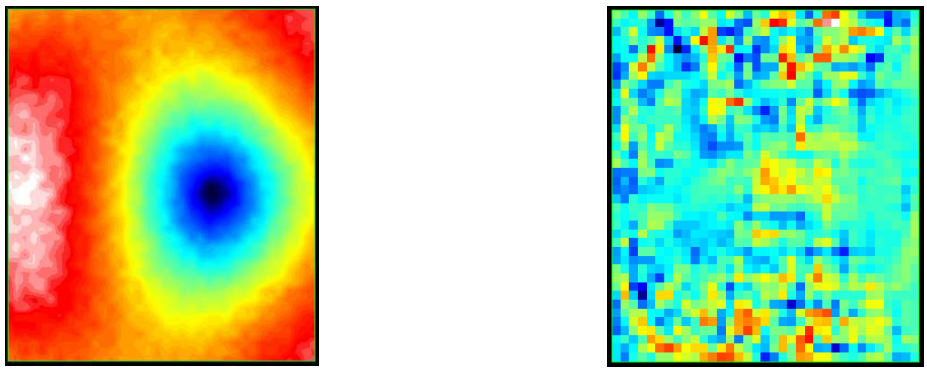

FIGURE 8. With 5% noise on the local data ($36 \times 41$ pixels), the reconstruction crashes.

We performed the same test on the local data. We aim to investigate the stability of the separation of scales when the data is noisy. We observed that the method was quite unstable on the local data, this was because the fine information of the local data is coded in high spatial frequencies, and consequently the information was significantly disturbed by the noise.
One could ask the question of the optimal size of the subregion, where we implement the method, in order to gain accuracy of the reconstruction, and to keep stability. The natural answer is the wavelength of the problem understood as $(\frac{\rho\omega^2}{\mu_{\text{typical}}})^{-\frac{1}{2}}$. The subregion should probably have a size of the same order as the wavelength.

### 3.2. **Local or global reconstruction ?**

As already noticed, this inverse problem is essentially local in the sense that local data determine local solution. An another way to see this is to consider that because the data is available over the all domain, the problem is posed in the same way, wether one considers $\Omega$ or $\Omega' \subset \Omega$, or $\Omega'' \subset \Omega'$. The most local approach would be to estimate locally the derivatives of $\mathbf{u}^*$, with a local finite difference scheme. That is the method referred to in 1.2.
Yet in practice, the inverse problem is not:

$$\mathbf{u}(x) \rightarrow \mu(x)$$

but rather:

$$\mathbf{S_h}[\mathbf{u}(\mathbf{x}) + \delta\mathbf{W}(\mathbf{x})] \rightarrow \mu(\mathbf{x})$$

where $W$ is additive noise, and $\mathbf{S_h}$ is a sampling operator. This modification imposes to take advantage of the spatial coherence of the wavefield. Because the local reconstruction is unstable, one has to make a trade off between stability and accuracy: The smaller the data-sets you consider, the better is the accuracy, but the less stable the method becomes. The consequence of this in purely local reconstructions like (2), is that one has to interpolate and smooth the data in order to make the computation more stable, and this smooth interpolation process requires to consider the data in a neighborhood of the point of interest.

### 3.3. **Regularization of the local reconstruction**

In order to stabilize the local reconstruction, we minimized a regularized functional:

$$J_{\text{reg}}(\mu) = J(\mu) + \beta \int_\Omega |\nabla\mu(x)|dx.$$

The gradient of the regularization term, which is the total variation of the shear modulus map, is known:

$$\frac{\partial TV(\mu)}{\partial \mu} = -\int_\Omega \nabla.(\frac{\nabla\mu}{|\nabla\mu|})dx.$$

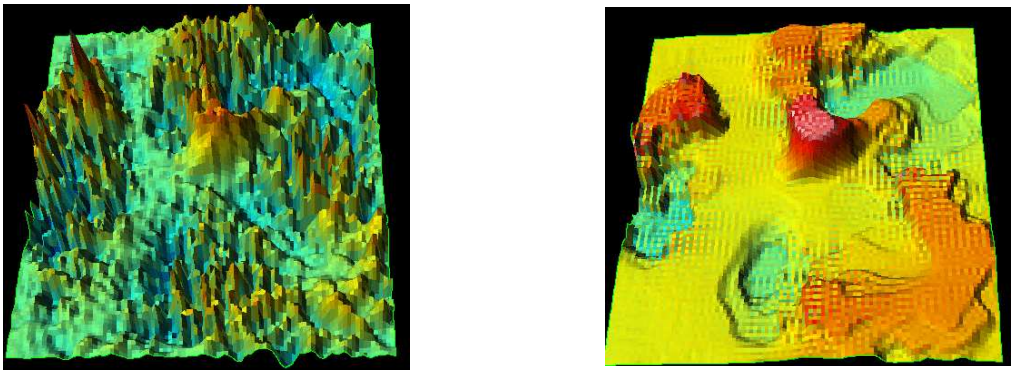

FIGURE 9. Local reconstruction of an inclusion without regularization (Left), and with regularization (Right). The inclusion in more visible with the regularized reconstruction.

With this modified gradient, we had the results of Fig. 9.

Although we see some regularization on the results, the parameters $\beta$ and $\delta_0$ are quite tricky to tune.

## 4. Conclusion and perspectives

We supported the idea that treating scales independently is essential to achieve maximal resolution. For us, this was practically done by performing the analysis on small sub-zones. We would like to know wether it is possible to process the spatial spectrum of the data directly in order to avoid the painful handling of sub-zones. Multi-scale techniques such as wavelets might be of some help although the technical handling of multi-scale tools are not easy in the framework of finite elements.

## References

[1] H. Ammari, P. Garapon, H. Kang and H. Lee, A Method of biological tissues elasticity reconstruction using magnetic resonnance elastography measurements, Quart. Appl. Math., 66 (2008), 139–175.

[2] T.F. Chan and X.-C. Tai, Level set and total variation regularization for elliptic inverse problems with discontinuous coefficients, J. Comput. Phys., 193 (2003), 40–66.

[3] J.F. Greenleaf, M. Fatemi, and M. Insana, Selected methods for imaging elastic properties of biological tissues, Annu. Rev. Biomed. Eng., 5 (2003), 57–78.

[4] R. Sinkus, J. Lorenzen, D. Schrader, M. Lorenzen, M. Dargatz, and D. Holz, High-resolution tensor MR elastography for breast tumour detection, Phys. Med. Biol., 45 (2000), 1649–1664.

[5] R. Sinkus, M. Tanter, S. Catheline, J. Lorenzen, C. Kuhl, E. Sondermann, and M. Fink, Imaging anisotropic and viscous properties of breast tissue by magnetic resonance-elastography, Mag. Reson. Med., 53 (2005), 372–387.

[6] R. Sinkus, M. Tanter, T. Xydeas, S. Catheline, J. Bercoff, and M. Fink, Viscoelastic shear properties of in vivo breast lesions measured by MR elastography, Mag. Res. Imag., 23 (2005), 159–165.

[7] J. Bercoff, M. Tanter, M. Fink Supersonic Shear Imaging: a new technique for soft tissues elasticity mapping IEEE Trans. UFFC., 51 (2004), 374–409.

[8] F. Ihlenburg *Finite Elements Analysis of Acoustic Scattering* - Springer, New York, 1998.

[9] E.E.W. Van Houten, K.D. Paulsen, M.I. Miga, F.E. Kennedy, and J.B. Weaver An Overlapping Subzone Technique for MR-Based Elastic Property Reconstruction Mag. Reson. Med., 42 (1999), 779–786.

[10] E.E.W. Van Houten, M.M. Doyley, F.E. Kennedy, J.B. Weaver, and K.D. Paulsen Initial In Vivo Experience with Steady-State Subzone-Based MR Elastography of the Human Breast J. Magn. Reson. Imag., 17 (2000), 72–85.